Special issue: ICAMSF2025

Institution of MECHANICAL ENGINEERS
Journal of ENGINEERING TRIBOLOGY

Tribological performance optimization of AZ91/TiB_2 magnesium matrix composites using stacked ensemble learning and Bayesian methods

Proc IMechE Part J:
J Engineering Tribology
1–18

DOI: 10.1177/13506501251377565
journals.sagepub.com/home/pij
Sage

Sathish Kamaraj[1], Baskar Sanjeevi[2], Hariharasakthisudhan Ponnarengan[3], Logesh Kamaraj[4] and Sathickbasha Katharbasha[5]

Abstract

This work aims to develop and optimize lightweight, wear-resistant AZ91 magnesium matrix composites reinforced with titanium diboride (TiB_2) for demanding tribological applications. A hybrid ultrasonic-assisted mechanical stir casting technique was used to fabricate composites with 0–4 wt.% TiB_2, ensuring uniform reinforcement dispersion. The tribological behavior was systematically evaluated under dry sliding conditions using a Taguchi L18 orthogonal design with sliding speed, normal load, and TiB_2 content as variables. To address the nonlinear interdependencies among these factors and predict key tribological responses, wear rate (WR) and coefficient of friction (COF), a stacked ensemble learning (SEL) model was developed, integrating random forest, gradient boosting, and a polynomially expanded meta-regressor. The SEL model achieved high prediction accuracy ($R^2 = 0.948$ for COF, 0.908 for WR). Subsequently, Bayesian Optimization (BO) based on Gaussian Process Regression was employed for multi-objective process parameter optimization. The optimal combination—13.77 N normal load, 1.94 m/s sliding speed, and 3.98 wt.% TiB_2, yielded experimentally validated WR and COF values of 10.235 mg/km and 0.326, with <5% deviation from predictions. SEM analysis revealed mild abrasive wear, delamination and localized grain refinement as key mechanisms. This study conclusively demonstrates the efficacy of coupling advanced machine learning with experimental validation for intelligent design of Mg-based composites. The proposed SEL–BO framework reduces experimental workload while ensuring high-performance tribological outcomes, supporting its application in aerospace and automotive systems where both weight and surface durability are critical.

Keywords

AZ91 magnesium matrix composite, tiB_2 reinforcement, stacked ensemble learning, Bayesian optimization, tribological performance

Received: 25 April 2025; accepted: 25 August 2025

Introduction

The growing demand for advanced lightweight structural materials with engineered surface durability has driven intensive research into magnesium matrix composites (MMCs), particularly for tribological applications such as automotive braking systems, aerospace actuators, and precision electromechanical interfaces. Magnesium alloys are currently the second most researched category among light metal matrix composites, following aluminum-based systems, due to their promising strength-to-weight ratio, corrosion resistance, and application potential across automotive, aerospace, military, electronic, and biomedical sectors.[1] Among magnesium alloys, AZ91 (Mg–9Al–1Zn) has received considerable attention due to its high specific strength, excellent castability, and corrosion resistance. However, AZ91 exhibits significant wear degradation under dry sliding, stemming from its low hardness, high reactivity, and limited resistance to thermal softening and plastic deformation under localized loads.[2]

[1]Department of Mechanical Engineering, Vels Institute of Science Technology and Advanced Studies, Chennai, Tamil Nadu, India
[2]Department of Automobile Engineering, Vels Institute of Science, Technology & Advanced Studies, Chennai, Tamil Nadu, India
[3]Department of Mechanical Engineering, Dr Mahalingam College of Engineering and Technology, Pollachi, Tamil Nadu, India
[4]Department of Mechanical Engineering, Vel Tech Rangarajan Dr Sagunthala R&D Institute of Science and Technology, Chennai, Tamil Nadu, India
[5]Department of Mechanical Engineering, B.S. Abdur Rahman Crescent Institute of Science and Technology, Chennai, Tamil Nadu, India

Corresponding authors:
Baskar Sanjeevi, Research Supervisor, Department of Automobile Engineering, Vels Institute of Science, Technology & Advanced Studies, Chennai - 600 117, Tamil Nadu, India.
Email: baskar133.se@vistas.ac.in

Hariharasakthisudhan Ponnarengan, Associate Professor (Research), Department of Mechanical Engineering, Dr Mahalingam College of Engineering and Technology, Pollachi–642 003, Tamil Nadu, India.
Email: harimeed2012@gmail.com

To mitigate these deficiencies, researchers have increasingly turned to metal matrix nanocomposites (MMNCs), which offer customizable mechanical and tribological properties. Jovana Krstić et al. underscored the need for international standards to guide MMNC development and ensure application consistency.[3] Kothuri Chenchu Kishor Kumar et al. applied artificial neural networks (ANN) to predict wear and friction in AZ31-SiC composites with high precision, recording errors of just 4.71% for wear and 5.79% for the coefficient of friction, highlighting the value of machine learning in materials science.[4] In the biomedical field, Sachin Kumar Sharma et al. utilized spark plasma sintering to improve corrosion resistance and mechanical integrity in Mg–Ti alloys, with the Mg80-Ti20 composition showing superior performance and biocompatibility.[5]

Shifting focus to automotive components, Vencl, Aleksandar et al. reviewed Al–Si-based MMCs and found that A356 composites reinforced with Al_2O_3, SiC, and graphite via compocasting outperformed traditional gray cast iron in wear-critical applications.[6] A.P. Sannino et al. introduced a tribological framework distinguishing surface, subsurface, and third-body effects to elucidate wear behavior across studies.[7] Aleksandar Vencl et al. demonstrated that A356 reinforced with 3 wt.% Al_2O_3 improved dry sliding wear resistance significantly.[8] Enhancement of AZ91's tribological behavior has also been pursued through ceramic reinforcements. Hemendra Patle et al. showed that B_4C reinforcement reduced wear by 60% and limited oxidation-induced friction under inert conditions.[9] Aatthisugan I et al. achieved a 52.2% wear loss reduction by integrating B_4C and graphite, validating the benefits of hybrid reinforcement.[10] Niranjan C. A. et al. further improved wear resistance using 1.5–2 wt.% Al_2O_3 nanoparticles, emphasizing the role of particle composition and test parameters.[11]

Expanding this approach, Mohammad Zarghami et al. incorporated 10% SiC into AZ91–Mg_2Si, forming protective oxide layers and cutting wear by 54% at 200 °C.[12] Anil Kumar et al. employed 3–12 wt.% TiC to enhance microstructure and frictional stability,[13] while Praveen Raj P. et al. validated a 36.16% wear volume reduction with a 9% SiC–3% BN hybrid.[14] Dinesh Kumar et al. used ultrasonic-assisted casting with 2.25 wt.% Al_2O_3 to ensure uniform dispersion, boosting wear performance.[15] However, excessive SiC content, as noted by later studies,[16] may hinder matrix compliance under high loads. Amin Abdollahzadeh et al. overcame this by using friction stir vibration for uniform SiC distribution, improving both strength and wear resistance by ∼15%.[17] Bharathi M. L. et al. observed similar enhancements with 2 wt.% Al_2O_3 in AZ91D.[18] For high-temperature applications, Annamalai Gnanavelbabu et al. found 1% TiO_2 yielded optimal wear and friction response below 150 °C.[19] Peng Xiao et al. refined Mg_2Si morphology via Sb modification, reducing wear and corrosion by 26% and 52.8%, respectively.[20] Sakshi Singh et al. achieved enhanced wear resistance with 2–6 wt.% B_4C,[21] and Mohammad Goodarzi et al. leveraged CNTs' lubricating and hardening properties to reduce mass loss and friction.[22]

Artificial intelligence has been integral to recent advancements. Nikolaos A. Fountas et al. applied Grey Wolf and Whale Optimization to A356/Al_2O_3 composites, enabling effective multi-parameter optimization.[23] Blaža Stojanović et al. developed a hybrid ANN–RSM–GA–PSO model for wear prediction,[24] and Aleksandar Vencl et al. showed ANN outperforming RSM in wear prediction of ZA-27/alumina systems ($R^2 = 0.98729$).[25] Leonard Maduabuchi Akuwueke et al. demonstrated that surface texturing in epoxy composites with activated carbon improved tribological outcomes despite minor mechanical trade-offs.[26] In addition to artificial neural networks (ANNs), the application of genetic algorithms (GAs), particle swarm optimization (PSO), response surface methodology (RSM), and Box–Behnken design (BBD) are found as frequently employed methods in material behavior modeling and parameter optimization.

In the context of TiB_2-reinforced AZ91 systems, Peng Xiao et al. and B.N. Sahoo et al. confirmed wear resistance improvements through grain refinement and work hardening.[27,28] Xin Sui et al. identified optimal mechanical properties with 5 wt.% TiB_2 for strength and 15 wt.% for wear resistance.[29] Dinesh Kumar et al. reiterated the benefits of ultrasonic-assisted dispersion of TiB_2,[30] while Engin Cevik et al. enhanced AZ91 properties further by co-reinforcing with graphene.[31] S.K. Sahoo validated the high-temperature stability of TiB_2 in ZE41 alloys.[32]

Computational modeling continues to drive predictive capability. Harish Kruthiventi S. S. et al. found decision trees most accurate among ANN, ANFIS, and DT models for AZ91 wear.[33] Akshansh Mishra et al. demonstrated superior predictive power of a PSO-GBR hybrid for AZ31 wear ($R^2 = 0.99970$).[34] Cevher Kursat Macit et al. achieved 98.8% accuracy with a GA-SVR model,[35] and Fatih Aydin et al. reinforced ANN's predictive robustness for AZ91.[36] Mahammod Babar Pasha et al. verified the influence of uniform dispersion in reducing wear and friction using five ML models.[37] In process optimization, Dinesh Kumar et al. used Taguchi–GRA for optimizing TiB_2/AZ91D processing conditions,[38] while Mathivanan K. et al. reduced porosity in NiCr-coated AZ91D using DBN–Mayfly with RSM.[39] Veera Ajay C. et al. optimized AZ31–Al_2O_3/Si_3N_4 composites via RSM and ANN,[40] and Vignesh C. et al. applied GRA–ANN to model wear in Mg–2Zn–1Mn/β-TCP implants.[41] Sudhir Kumar et al. confirmed that load is the dominant parameter influencing wear and friction in AZ91–TiC–rGO systems3.[42]

Ensemble learning further refines prediction accuracy. Yanqiu Xia et al. applied Bayesian-optimized stacking models to amide and lithium-based grease with high R^2 values.[43,44] S. Kumaravel et al. used ANN–LSTM hybrids to predict wear in HEA-reinforced Al5083 with excellent reliability.[45] Poornima Hulipalled et al. found extreme gradient boosting most effective for Mn–ZA-27 alloys.[46] Xiaoxi Mi et al. applied Bayesian optimization to design Mg–Mn alloys with superior tensile strength.[47] M. Ghorbani et al. introduced a user-friendly multi-objective design platform using Gaussian processes,[48] while Peng Peng et al. used explainable ML to optimize biodegradable Mg alloys, identifying Zn content and extrusion temperature as key variables.[49]

Despite these advances, current AZ91 research predominantly relies on conventional processing and single-response optimization, neglecting multi-factorial interactions and underutilizing ensemble learning in integrated modeling frameworks. Addressing this, the present work synthesizes AZ91/TiB_2 composites via ultrasonic-assisted stir casting,

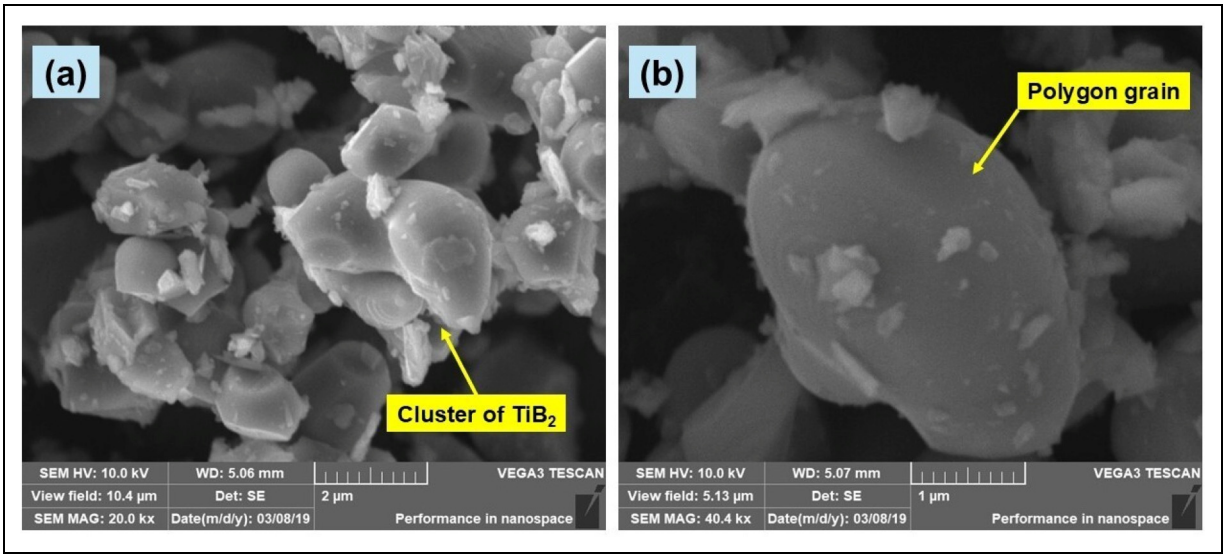

Figure 1. SEM images of TiB2 particles.

evaluates tribological responses using Taguchi L18 design, and constructs a stacked ensemble learning model combining random forest, gradient boosting, and polynomial regression for wear and friction prediction. Bayesian optimization with Gaussian process regression is employed to identify optimal tribological conditions. this study presents a hybrid AI-driven methodology coupling experimental validation with predictive modeling. This integrated framework offers a robust, scalable approach for designing tribologically superior lightweight MMCs tailored to aerospace and automotive demands.

Materials and methods

The matrix material used in this study was AZ91 magnesium alloy, sourced from accredited vendors in Chennai, India. AZ91, known for its high specific strength and corrosion resistance, serves as a viable matrix for wear-critical applications. Titanium Diboride (TiB_2) ceramic particles, procured from Sigma Aldrich with a purity of 99.9%, were employed as reinforcements. Scanning electron microscopic images in Figure 1(a) and (b) revealed that the TiB_2 particles exhibit a polygonal morphology with distinct angular grains and occasional clustering. The average particle size was estimated to be in the range of 1–3 µm, which is optimal for effective dispersion and interfacial stress transfer within the AZ91 matrix. The angular geometry of TiB_2 enhances mechanical interlocking, while its high hardness resists micro-ploughing during sliding. This tailored reinforcement strategy aims to improve wear resistance through structural rigidity and load-bearing synergy, making the AZ91/TiB_2 composite system suitable for tribological performance optimization.

Synthesis and microstructure of AZ91/TiB_2 composites

The AZ91/TiB_2 composites were fabricated using an integrated ultrasonic-assisted and mechanical stirring-based stir casting technique, designed to ensure homogeneous dispersion of reinforcement particles within the matrix. AZ91 alloy ingots were initially charged into a graphite crucible and melted in an electric resistance furnace at 720 °C under a protective argon atmosphere to minimize oxidation. Once fully molten, the alloy was superheated to 750 °C to facilitate wettability enhancement and accommodate the subsequent introduction of ceramic particulates. Pre-weighed TiB_2 particles were preheated to 350 °C for 60 min to eliminate moisture and thermally equilibrate the particles with the melt. The reinforcement was gradually introduced into the vortex generated by mechanical stirring at 600 r/min for 10 min using a stainless-steel impeller coated with zirconia to prevent interfacial reactions. Concurrently, an ultrasonic probe operating at a frequency of 20 kHz and power of 1 kW was immersed into the melt for 3 min to break up agglomerates and promote uniform dispersion through cavitation-induced microstreaming. Post-stirring, the composite melt was cast into preheated metallic molds at 200 °C to avoid thermal shock and promote directional solidification. This hybrid stirring approach significantly improves matrix-reinforcement wetting, minimizes clustering, and establishes a refined microstructure essential for superior wear performance.

The microstructural analysis shown in Figure 2 provides compelling evidence of the uniform dispersion of TiB_2 particles and their role in inducing significant grain refinement within the AZ91 matrix. Figure 2(a), acquired at 250× magnification using SE2 detection under an accelerating voltage of 12.00 kV, reveals a highly refined α-Mg matrix structure interspersed with TiB_2-rich regions. These regions appear as distinct bright contrast zones, indicating successful integration of the reinforcement within the matrix. The effective dispersion is attributed to the ultrasonic-assisted stir casting process employed in this study, wherein preheated TiB_2 particles were incorporated at 720 °C with continuous mechanical stirring at 600 r/min for 10 min, followed by ultrasonic vibration at 20 kHz for 3 min. This dual-action approach enhanced particle–matrix wetting and broke up initial agglomerates, facilitating uniform TiB_2 distribution even at higher loading fractions. The presence of TiB_2 at the inter-

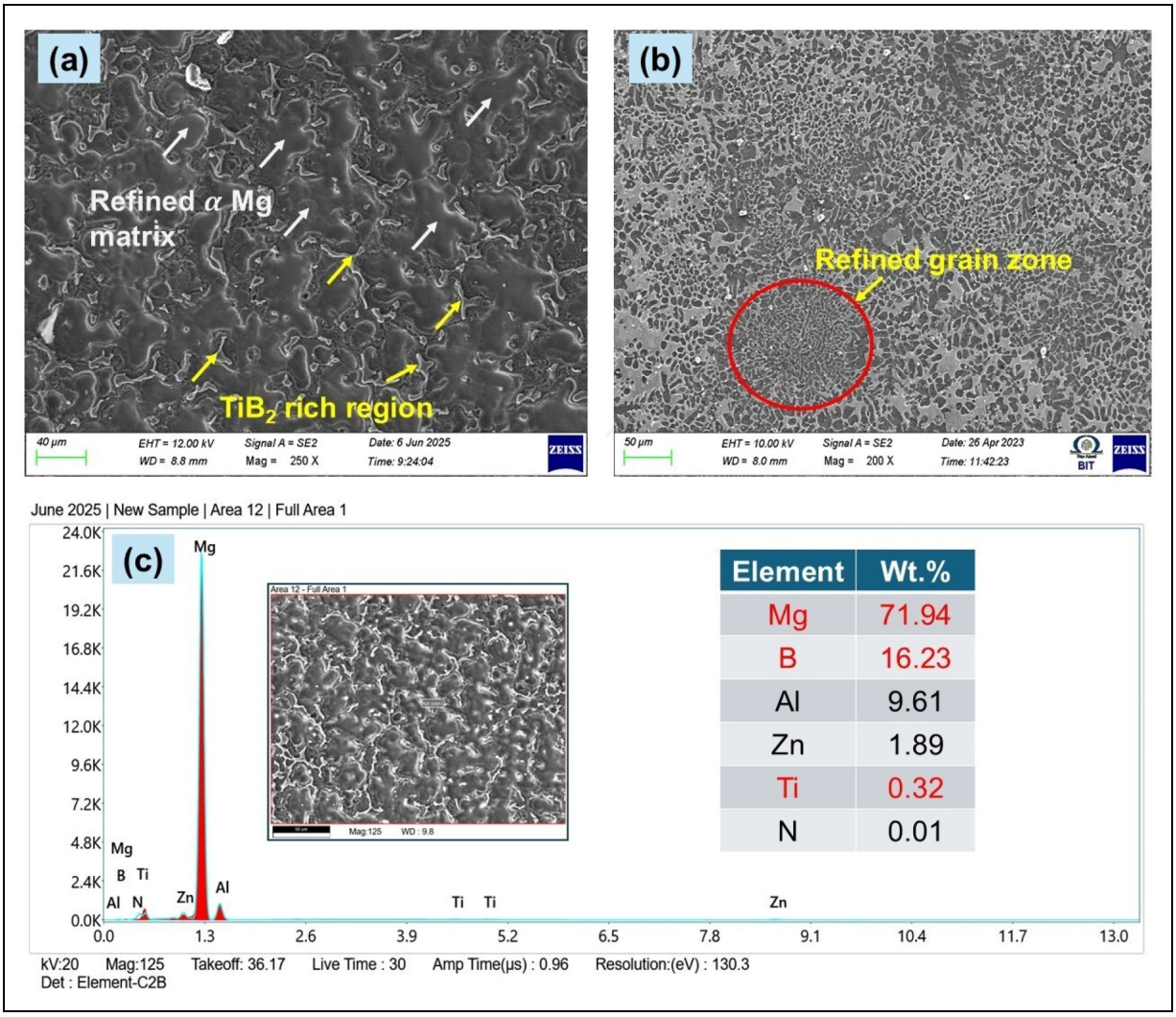

Figure 2. (a) SEM image showing refined α-Mg matrix and TiB_2-rich regions; (b) refined grain zone indicating nucleation effect; (c) EDS spectrum and elemental composition confirming presence of Ti and B.

dendritic and grain boundary regions acts as physical barriers to grain growth, contributing to heterogeneous nucleation and reduced α-Mg grain size.

Figure 2(b), taken at 200× magnification, distinctly highlights a refined grain zone surrounded by coarser α-Mg regions. This localized refinement correlates with the thermodynamically favorable nucleation of solid Mg on TiB_2 surfaces, which exhibit a low interfacial energy with the magnesium matrix due to good crystallographic compatibility. The suppressed growth of secondary dendrites and the spheroidized grain morphology observed in this zone confirm the efficiency of TiB_2 in pinning the solid–liquid interface during directional solidification.

In support of the morphological observations, Figure 2(c) presents an EDS spectrum acquired from the matrix zone. The corresponding quantitative analysis confirms the presence of Ti (0.32 wt.%) and B (16.23 wt.%), validating the retention of TiB_2 within the composite post solidification. The elemental mapping also indicates uniform Ti signal distribution, which aligns with the observed dispersion in SEM micrographs. The Al and Zn contents of 9.61 wt.% and 1.89 wt.%, respectively, suggest the stabilization of intermetallic phases typically found in AZ91 alloys. The combined microstructural and compositional evidence reaffirms the role of TiB_2 as an effective grain refiner and thermally stable reinforcement, which enhances structural integrity and contributes directly to the improved tribological performance discussed in subsequent sections.

To support the evaluation of tribological performance, fundamental material properties, Brinell hardness, density, and porosity, were determined for the fabricated AZ91/TiB_2 composites. The Brinell hardness (BHN) was measured according to ASTM E10 using a 2.5 mm steel ball and 62.5 kgf load applied for 30 s. Density was identified using the Archimedes principle, while theoretical density was calculated using the rule of mixtures. Porosity (%) was computed based on the deviation between theoretical and measured densities. The results are summarized in Table 1.

As observed, hardness improved progressively with the increase in TiB_2 reinforcement, from 63 BHN in the unreinforced alloy to 74 BHN in the 4 wt.% TiB_2 composite. This enhancement is due to the inherent high hardness of TiB_2 particles, which act as barriers to localized plastic deformation and contribute to the formation of a stronger load-bearing matrix. Measured densities also increased with reinforcement, indicating the replacement of lighter magnesium regions with denser ceramic inclusions. Porosity decreased

Table 1. Brinell hardness, density, and calculated porosity of AZ91/TiB_2 composites.

TiB_2 Content (wt.%)	Brinell Hardness (BHN)	Measured Density (g/cm³)	Theoretical Density (g/cm³)	Porosity (%)
0	63	1.78	1.81	1.66
2	71	1.83	1.86	1.61
4	74	1.89	1.91	1.05

Table 2. Taguchi's L18 orthogonal array.

Exp. Run	Sliding speed (m/s)	Normal load (N)	TiB_2 (Wt.%)
1	1	10	0
2	1	10	2
3	1	10	4
4	1	20	0
5	1	20	2
6	1	20	4
7	1	30	0
8	1	30	2
9	1	30	4
10	2	10	0
11	2	10	2
12	2	10	4
13	2	20	0
14	2	20	2
15	2	20	4
16	2	30	0
17	2	30	2
18	2	30	4

consistently, reflecting improved wettability, reduced clustering, and enhanced particle-matrix bonding, attributed to the effectiveness of the ultrasonic-assisted stir casting process.

Design of experiment and test methods

A structured Design of Experiments (DOE) was developed using Taguchi's L18 orthogonal array as represented in Table 2, to assess the tribological performance of AZ91/TiB_2 composites. The primary input parameters sliding speed (1 and 2 m/s), normal load (10, 20, and 30 N), and TiB_2 content (0, 2, and 4 wt.%) were selected based on their known influence on interfacial shear, wear mechanisms, and surface degradation in particle-reinforced magnesium alloys. In this study, cylindrical specimens with a 6 mm diameter and hemispherical tip were used. For pressure estimation, the projected contact area of the hemisphere was approximated using the circular cross-sectional area of the specimen, i.e., 28.27 mm². Based on this, the applied normal loads of 10 N, 20 N, and 30 N correspond to contact pressures of 0.354 MPa, 0.707 MPa, and 1.061 MPa, respectively. The levels of each factor were finalized following a detailed pilot study that identified optimal process windows to avoid reinforcement clustering, matrix softening, and test noise variability. The chosen sliding speeds simulate typical boundary-to-mixed lubrication regimes, while the selected loads reflect realistic stress levels encountered in aerospace and automotive assemblies using lightweight components. The TiB_2 content was restricted to a maximum of 4 wt.% to ensure uniform dispersion and stable rheology during casting.

The selection of sliding speed, normal load, and TiB_2 content as input variables was guided by their combined influence on tribological performance under dry sliding conditions. While TiB_2 content is a material parameter determined during composite fabrication, sliding speed and normal load are operational variables that simulate real-world service conditions. This study aimed to integrate both material design and functional testing parameters into a unified predictive framework to evaluate how different TiB_2 loadings perform under varied mechanical and thermal stress regimes. Sliding speeds of 1–2 m/s and normal loads of 10–30 N were selected based on prior tribological literature and pilot experiments, representing typical boundary-to-mixed lubrication regimes in automotive and aerospace systems. Although no traditional processing parameters (e.g., melt temperature, stirring rate) were included in the modeling phase, the ultrasonic-assisted stir casting method was standardized across all specimens to isolate the effect of TiB_2 content and tribological test conditions. This strategy allowed the development of a robust data-driven model capable of guiding both composition and application-specific parameter optimization.

Tribological tests were carried out using a DUCOM pin-on-disc tribometer in accordance with ASTM G99 standards under dry sliding conditions at ambient temperature. Cylindrical specimens measuring 6 mm in diameter and 40 mm in length with a hemispherical tip were fabricated from each composite. The counter-body used for all tribological tests was stainless steel 316L with a machined surface roughness of $Ra < 5$ μm, Vickers hardness 183 ± 5 HV, and diameter of 100 mm. This level of roughness was intentionally selected to simulate practical dry sliding conditions encountered in real-world applications such as automotive braking systems, aerospace linkages, and structural interfaces, where surface finishing is often constrained by machining tolerances or in-service wear. A moderately rough counterface enables the activation of micro-ploughing, adhesive contact formation, and third-body abrasion mechanisms, which are critical to understanding the tribological performance of metal matrix composites under operational loads. The surface roughness (Ra) of the AZ91/TiB_2 composite test samples was measured using a contact-type profilometer (Mitutoyo SJ-210) prior to tribological testing. The average roughness was maintained between 0.8 and 1.2 μm, achieved through controlled machining followed by light surface finishing. This roughness level was selected to ensure consistent surface conditions across all samples, facilitate reliable pin-disc contact, and reflect realistic surface characteristics of cast and machined magnesium alloy components used in dry sliding applications. The ambient temperature during all tribological tests was maintained at 25 ± 2 °C under laboratory conditions. The sliding distance was maintained at a constant 1 km for all tribological tests conducted in this study. This test length was chosen to ensure sufficient material interaction for wear characterization while remaining consistent across all experiments for comparative accuracy. Frictional force was continuously recorded during the test, while wear was quantified through mass loss measurements using a Shimadzu AUW-D semi-microbalance with

0.01 mg resolution. This configuration enabled high-sensitivity capture of tribological responses under controlled, repeatable test conditions, aligning with the study's objective to model and optimize wear performance. The wear rate (WR) was determined using the standard mass loss method under dry sliding conditions, and it was calculated using the following expression:

$$Wear\ rate\ \left(\frac{mg}{km}\right) = \frac{\Delta m \times 1000}{d} \quad (1)$$

where 'Δm' is the mass loss in milligrams (mg) and d is the sliding distance in meters (m). All specimens were cleaned before and after each test using ethanol, and mass loss was measured. The resulting mass loss were then normalized with respect to the total sliding distance (1 km) to ensure consistency across all test conditions. In this study, the coefficient of friction (COF) was calculated exclusively from the steady-state region of the frictional profile, carefully excluding the initial run-in phase. The steady state was identified by observing the region where the COF values stabilized with minimal fluctuation, typically after the early adaptive interactions between the contact surfaces had subsided. To ensure repeatability and minimize experimental uncertainty, each tribological test condition defined in the Taguchi L18 design was repeated three times, and the average values of coefficient of friction and wear rate were reported. The consistency of the results was validated by monitoring standard deviations across trials.

Results and discussion

Taguchi analysis

A structured experimental plan based on the Taguchi L18 orthogonal array was adopted to study the tribological response of AZ91/TiB_2 composites. The matrix included combinations of sliding speed, normal load, and TiB_2 content to evaluate their effects on wear rate and coefficient of friction (COF). Table 3 summarizes the complete experimental results, which serve as the foundation for the subsequent analysis and discussion of parametric influences and optimization outcomes.

The influence of process parameters sliding speed (SS), normal load (NL), and TiB_2 content on the tribological responses of AZ91 magnesium matrix composites was evaluated through Taguchi's L18 orthogonal array. Table 4 presents the response table for means, where the delta values and associated ranks reveal the relative impact of each factor on the composite's wear performance.

Among the three factors, TiB_2 content exhibited the highest delta value (4.168), assigning it Rank 1, signifying its dominant influence on the wear behavior. The role of TiB_2 is pivotal in strengthening the matrix–reinforcement interface to sustain higher contact stresses. The angular and faceted morphology of TiB_2 particles, as observed in SEM images (Figure 1), plays a pivotal role in enhancing mechanical interlocking with the AZ91 matrix. The sharp edges and polygonal grains provide physical anchoring points during solidification, allowing the molten matrix to conform around the particle contours and establish an interlocked interface. This geometry improves load transfer efficiency, restricts interfacial debonding, and minimizes particle pull-out during sliding. Additionally, the irregular surface profile increases the effective interfacial area, further contributing to enhanced bonding strength and overall wear resistance of the composite. The sharp reduction in both wear rate (WR) and coefficient of friction (COF) with increasing TiB_2 content, as visualized in the interaction plots represented in Figure 3 and 4, substantiates its solid lubricant behavior and capacity to hinder plastic flow in the soft AZ91 alloy. These ceramic particulates act as micro-barriers, promoting a transition from adhesive to abrasive wear mechanisms.

Normal load was ranked second (delta = 2.633), wherein lower loads (10 N) consistently resulted in reduced WR and COF. This behavior is linked to reduced thermal and mechanical deformation of the AZ91 matrix under minimal stress. As NL increased, the real area of contact expanded, intensifying adhesive interactions and leading to material ploughing. This trend is apparent in the WR plot showed in Figure 3, where the wear increases linearly with load, particularly at lower TiB_2 contents.

Sliding speed, though statistically the least influential (delta = 0.864), still demonstrated a notable role in modulating interfacial temperature and oxidation-driven wear mechanisms. At lower speeds (1 m/s), both WR and COF were higher, likely due to inadequate heat dissipation and the dominance of metal-to-metal contact. In contrast,

Table 3. Results of response values of coefficient of friction and wear rate.

Exp. Run	Sliding Speed (m/s)	Normal Load (N)	TiB_2 (wt.%)	Coefficient of Friction	Wear Rate (mg/km)
1	1	10	0	0.43	18.5
2	1	10	2	0.39	14.8
3	1	10	4	0.35	11.2
4	1	20	0	0.47	22.1
5	1	20	2	0.41	16.9
6	1	20	4	0.36	13.4
7	1	30	0	0.5	25.6
8	1	30	2	0.43	19.3
9	1	30	4	0.38	15.2
10	2	10	0	0.41	16.3
11	2	10	2	0.37	13.1
12	2	10	4	0.33	9.9
13	2	20	0	0.45	19.8
14	2	20	2	0.39	15.4
15	2	20	4	0.34	12.1
16	2	30	0	0.48	23.2
17	2	30	2	0.42	17.5
18	2	30	4	0.37	14.3

Table 4. Response table for means from taguchi analysis.

Level	Sliding speed (SS) (m/s)	Normal load (NL) (N)	TiB_2 (wt%)
1	8.929	7.173	10.687
2	8.064	8.510	8.284
3		9.807	6.519
Delta	0.864	2.633	4.168
Rank	3	2	1

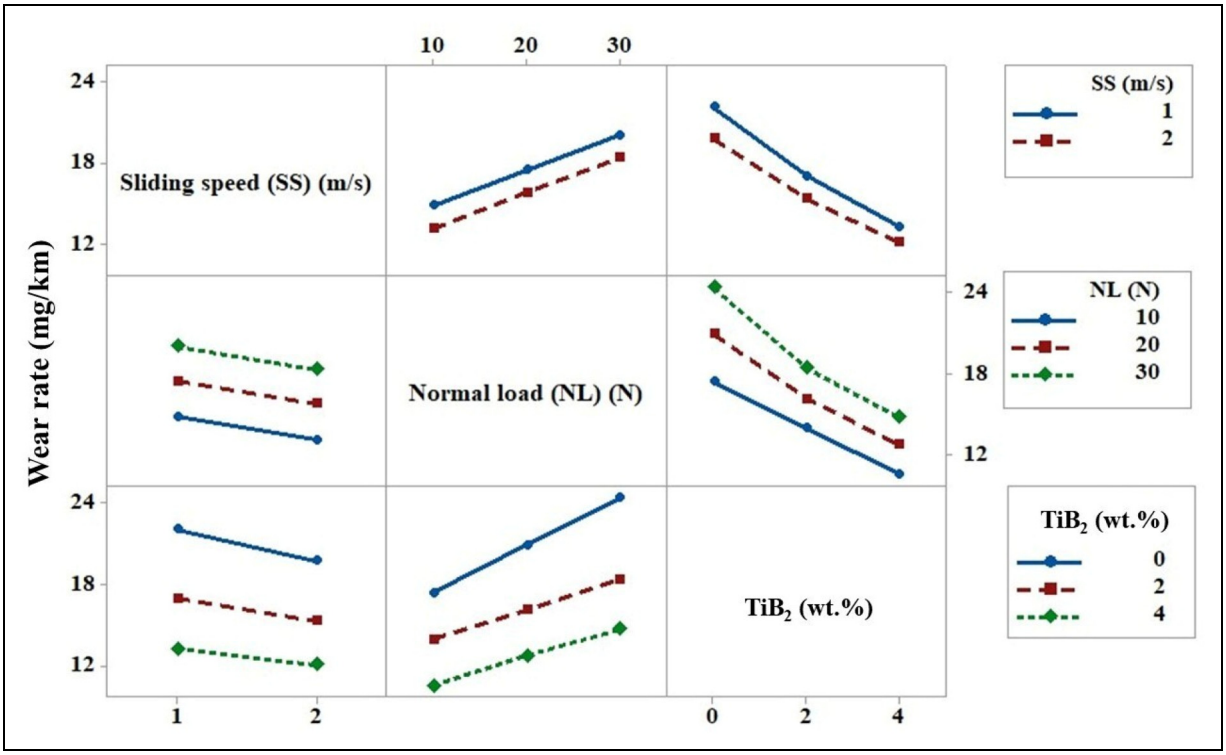

Figure 3. Interaction plot of data means for wear rate.

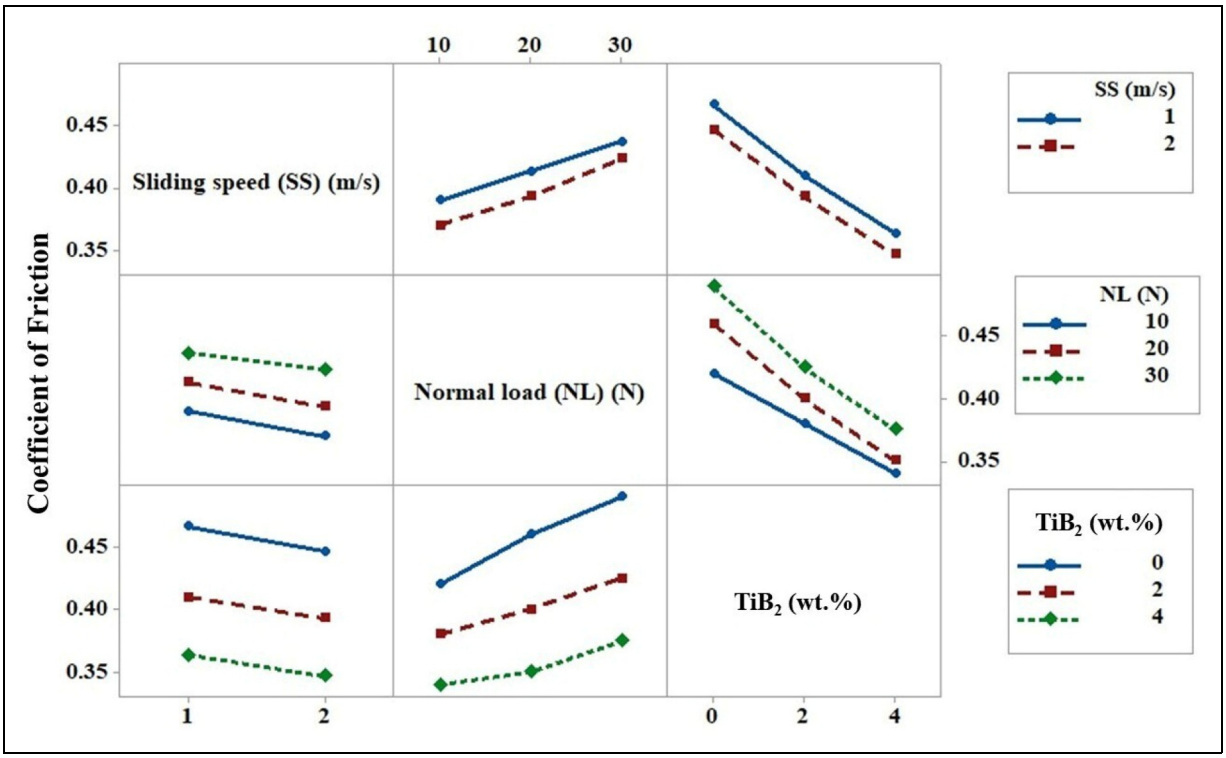

Figure 4. Interaction plot of data means for coefficient of friction.

elevated speeds favoured delamination and thermal softening, which facilitated smoother sliding with less material loss evident from the descending WR trends in Figure 3 with increasing speed. The interaction plots provide critical insight into the synergistic effects among factors. For instance, Figure 4 indicates that at 30 N and 4 wt.% TiB_2, the COF sharply declines, emphasizing the load-carrying capacity introduced by ceramic dispersion. Such nonlinear interactions underscore the need for a statistical design like Taguchi to dissect parameter interdependencies and conditions that minimize friction and wear properties.

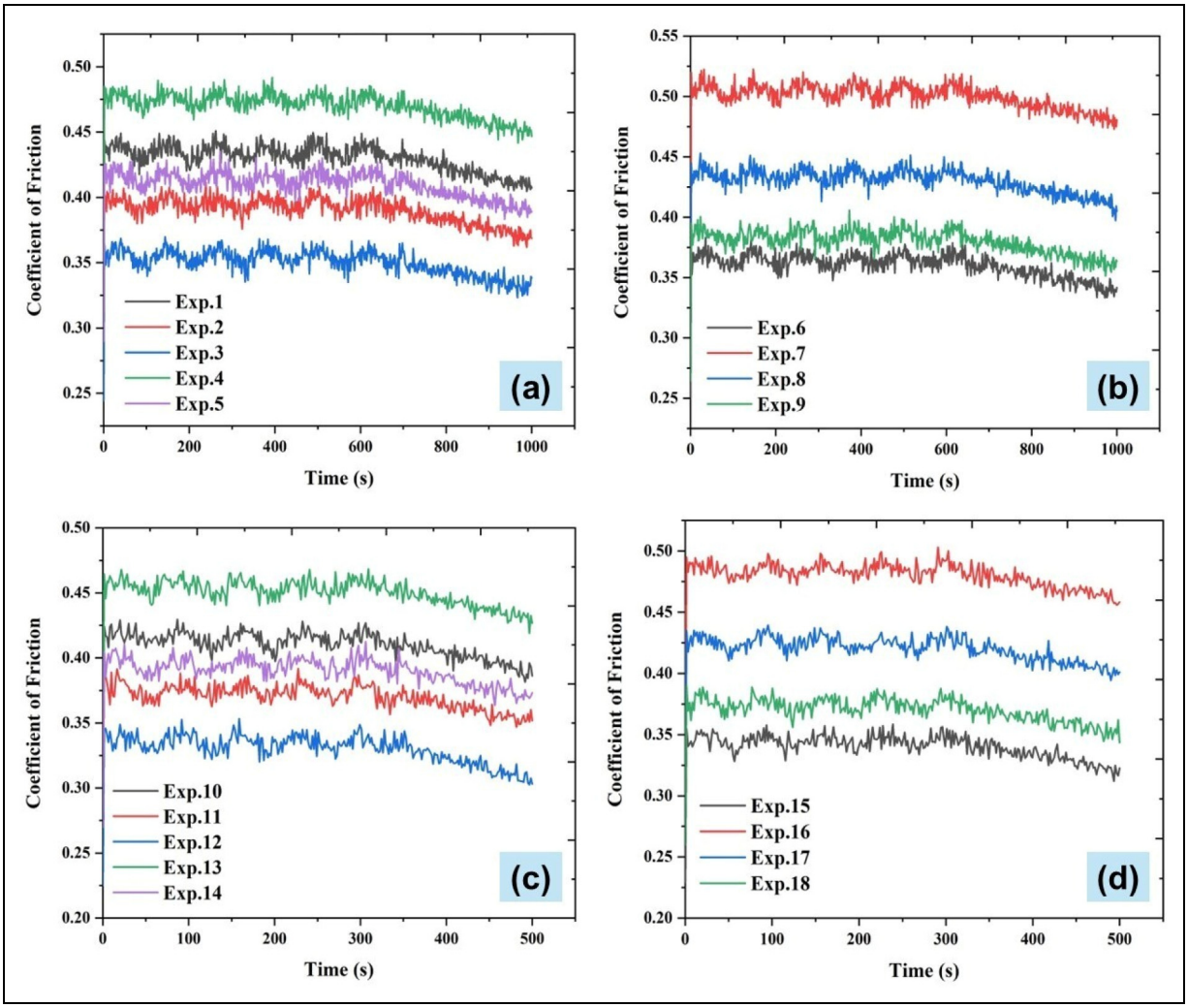

Figure 5. Variation of coefficient of friction with time for all 18 experimental runs: (a) Exp. 1–5, (b) Exp. 6–9, (c) Exp. 10–14, (d) Exp. 15–18.

Figure 5 presents the time-resolved coefficient of friction (COF) profiles for all 18 experimental runs, grouped as Exp. 1–5 (Figure 5(a)), Exp. 6–9 (Figure 5(b)), Exp. 10–14 (Figure 5(c)), and Exp. 15–18 in (Figure 5(d)). Each plot reveals a typical progression from an initial transient phase to a stabilized steady-state region. This validates the use of steady-state COF values, excluding early run-in effects as described in Section 2.2. In Figure 5(a), under low load (10 N), increasing TiB_2 content leads to a marked reduction in COF. Exp. 3 (4 wt.%) shows the most stable and lowest COF, whereas Exp. 1 (0 wt.%) exhibits higher fluctuations, indicating insufficient load-bearing reinforcement. Figure 5(b) under moderate load (20 N) shows increased instability in Exp. 7 (2 wt.%), while Exp. 9 (4 wt.%) displays improved frictional behavior due to better reinforcement dispersion.

At a higher sliding speed of 2 m/s (Figure 5(c)), Exp. 12 (4 wt.%) demonstrates a downward COF trend, likely from effective thermal softening resistance and dynamic surface smoothing. In Figure 5(d), under high load (30 N), Exp. 15 (0 wt.%) shows pronounced instability, while Exp. 18 (4 wt.%) maintains a low, consistent COF, indicating improved interfacial integrity. Furthermore, the comparative analysis of the plots reaffirms the dominant influence of TiB_2 content, followed by normal load and sliding speed, in shaping the tribological response, consistent with the Taguchi analysis

Stacked ensemble learning

In the current investigation focused on AZ91 magnesium alloy reinforced with TiB_2 ceramic particles, predicting tribological behavior under varying process conditions demands a robust, generalizable, and high-fidelity data-driven model. Traditional single-regressor approaches often suffer from overfitting or insufficient generalization when dealing with complex nonlinear relationships. Therefore, a stacked ensemble learning (SEL) strategy was adopted to integrate the strengths of multiple base learners and enhance prediction reliability for both wear rate (WR) and coefficient of friction (COF).

The architecture of the SEL model is illustrated in Figure 6, detailed further in Table 5. The SEL model consists of two base learners, random forest regressor and gradient boosting regressor, each optimized with number of estimators of 50 and random state of 0. Polynomial feature expansion (degree = 2, without bias term) was introduced to both base learners to capture interaction effects between sliding speed, normal load, and TiB_2 content. The outputs of these

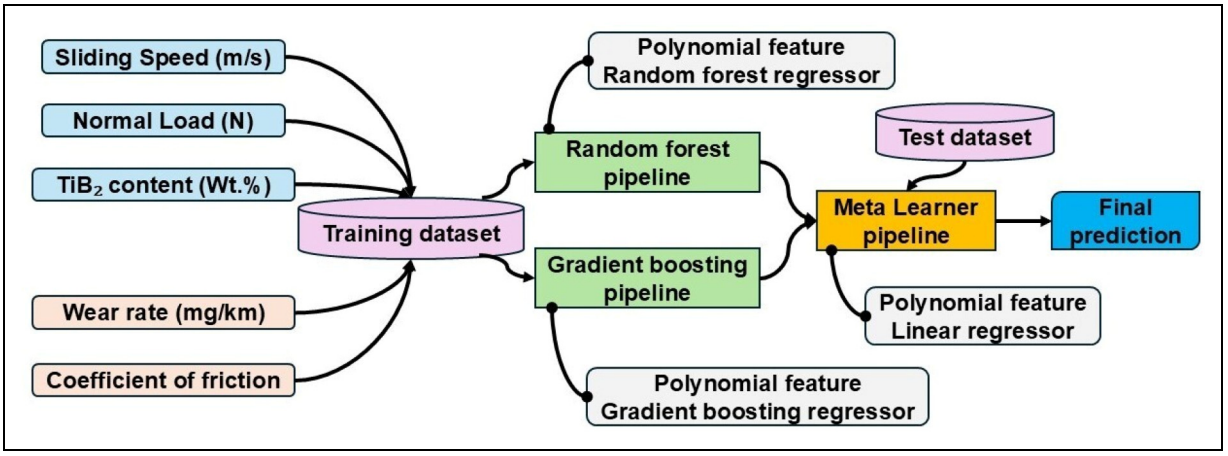

Figure 6. Model architecture of stacked ensemble model.

Table 5. Method and description of stacked ensemble modelling.

Component	Method	Description
Base Learner 1	Random forest regressor	- n_estimators = 50 - random_state = 0
Base Learner 2	Gradient boosting regressor	- n_estimators = 50 - random_state = 0
Polynomial Expansion (Base)	Polynomial features (in both base learners)	- degree = 2 - include_bias = False
Meta Learner	Linear regression	- Ordinary least squares regression
Polynomial Expansion (Meta)	Polynomial features	- degree = 2 - include_bias = False
Model Type	Stacking regressor (scikit-learn)	Ensemble of base learners with meta-learner
Target Variables	COF, WR	Separate stacked models built for each
Training Approach	In-sample fit (entire dataset used)	Training only

learners serve as meta-features, which are fed into a linear regressor meta-learner with an additional polynomial transformation, enabling it to model higher-order dependencies. The model was implemented using Scikit-learn's stacking regressor and trained using an in-sample approach.

The performance of the developed SEL model was validated using several key plots. Figure 7 depicts the scatter plots of predicted versus actual values for both WR and COF. The R^2 values 0.908 for WR and an outstanding 0.948 for COF, highlight the strong predictive power of the stacked model. These values confirm that the model can closely approximate experimental behavior across diverse input conditions.

Further insights are offered by the residual diagnostics in Figure 8(a) and (b). The residuals for both responses are symmetrically distributed around zero, indicating minimal systematic error or bias. Additionally, the histograms in Figure 8(c) and (d) confirm that the prediction errors are predominantly centered around zero, affirming the absence of skewed estimations and the model's statistical robustness.

The learning behavior of the gradient boosting base learner is presented in Figure 9(a) and (b). The clear convergence of training and testing MSE with increasing iterations indicates well-controlled generalization, without overfitting. This is particularly important given the moderate dataset size typical of experimental tribological studies. Feature importance analysis shown in Figure 9(c) and (d) reveals that TiB_2 content dominates the prediction of both WR and COF, followed by normal load and then sliding speed. This hierarchy aligns with the physical understanding that ceramic reinforcements primarily govern wear resistance and frictional performance by promoting load bearing interface, reducing plastic deformation, and enhancing surface hardness.

To validate the robustness of the stacked ensemble learning (SEL) model, its performance was compared against individual base learners, Random Forest Regressor (RF) and Gradient Boosting Regressor (GBR), using the same dataset and polynomial feature expansion (degree 2). The SEL model achieved higher in-sample R^2 values of 0.948 for COF and 0.908 for WR, compared to 0.912 (COF) and 0.871 (WR) for RF, and 0.925 (COF) and 0.887 (WR) for GBR, respectively. This improvement is attributed to the SEL architecture's ability to integrate diverse learning patterns from RF and GBR while capturing nonlinear interactions through the meta-regressor, thereby reducing both bias and variance. Additionally, the study considered the practical limitation of reinforcement content. While 4 wt.% TiB_2 was found optimal for tribological performance, higher contents could potentially lead to particle agglomeration due to increased melt viscosity and inadequate wetting. To counteract this, an ultrasonic-assisted stir casting method was employed, promoting de-agglomeration and homogeneous

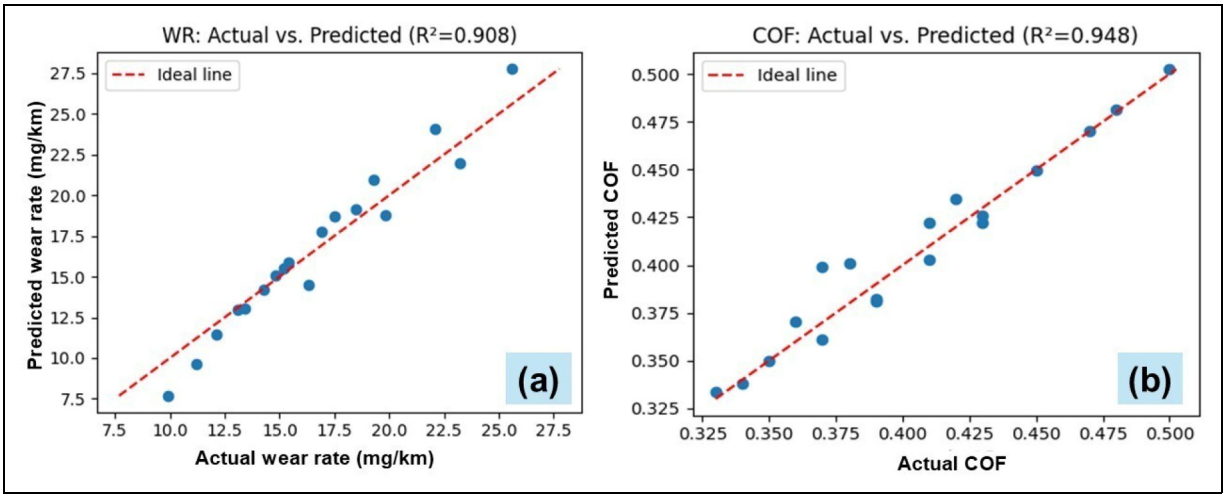

Figure 7. Actual vs predicted values of stacked ensemble model (a) wear rate (b) coefficient of friction.

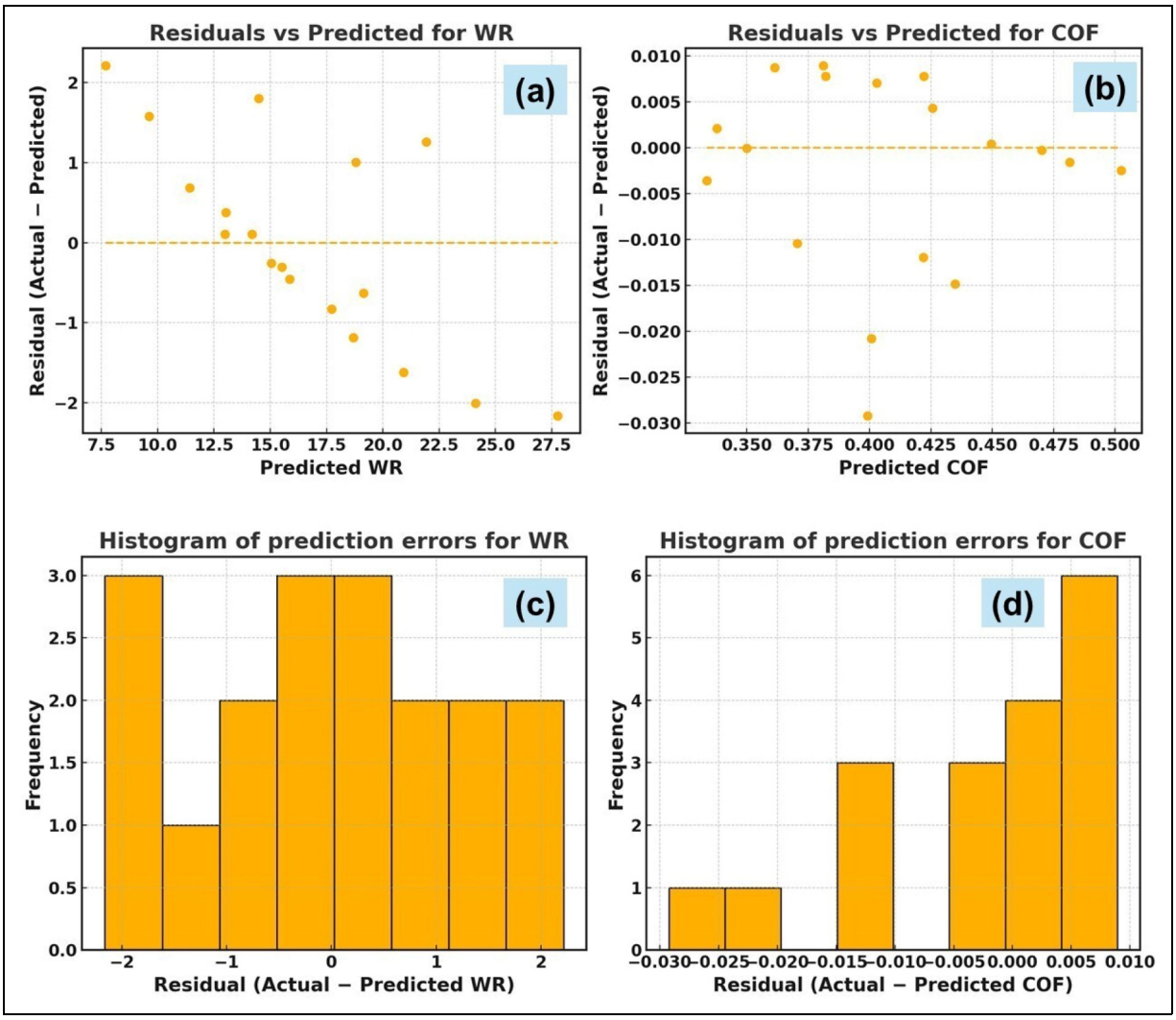

Figure 8. Residuals of actual and predicted values (a) wear rate (b) coefficient of friction; error histogram of (c) wear rate (d) coefficient of friction for stacked ensemble model.

dispersion of TiB_2 particles, which contributed to the observed wear resistance and frictional stability.

Regularization was intentionally omitted to maintain interpretability in the meta-regressor's coefficients. While cross-validation-based hyperparameter tuning was not implemented due to the limited dataset size (18 experiments), the SEL model exhibited high in-sample performance ($R^2 = 0.948$ for COF and 0.908 for WR), with uniformly

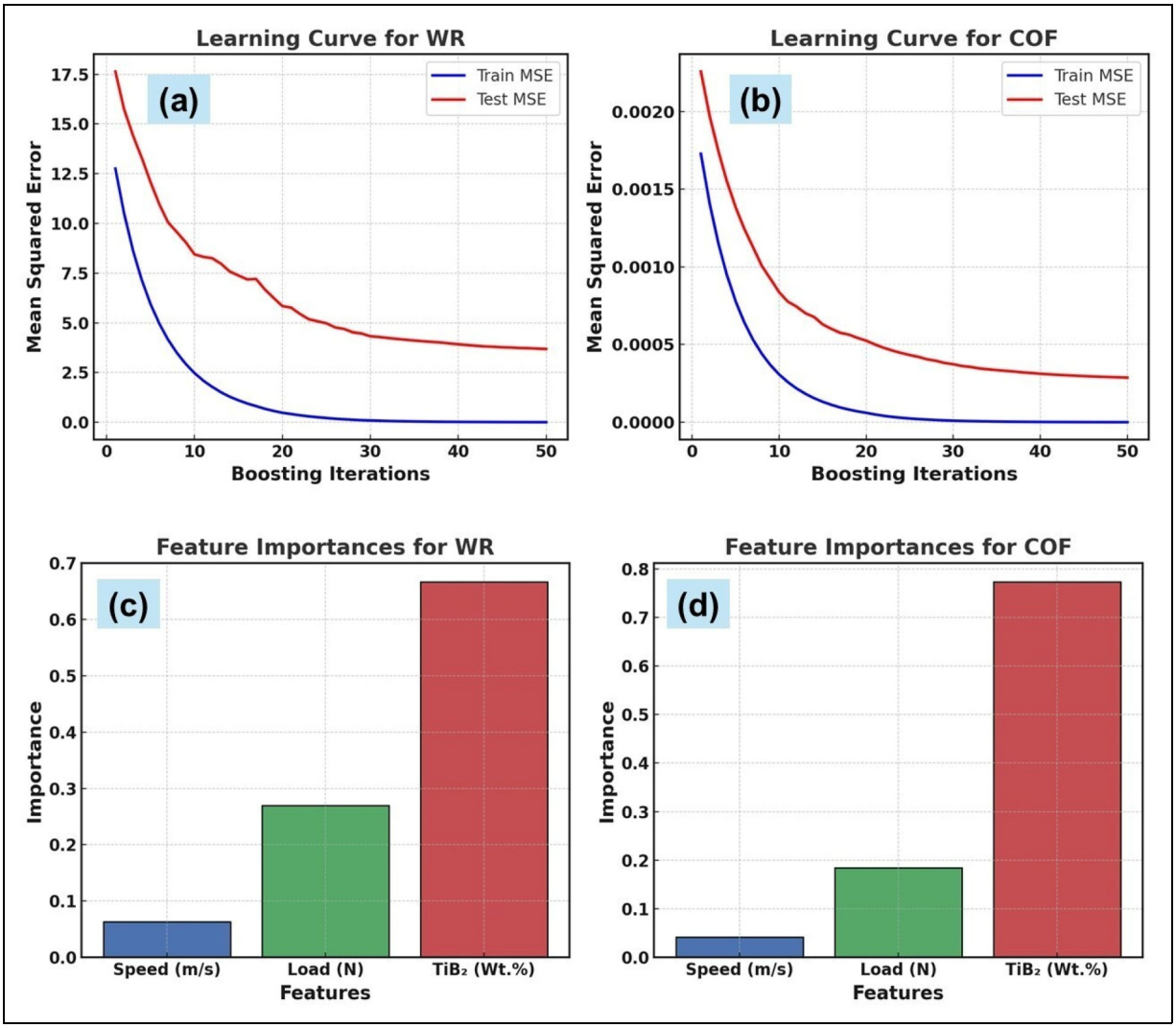

Figure 9. Learning curve of means squared error (a) wear rate (b) coefficient of friction; feature importances (c) wear rate (d) coefficient of friction for stacked ensemble model.

distributed residuals and minimal error, justifying the chosen configuration.

The correlation matrix presented in Figure 10 further corroborates these findings. TiB_2 content shows strong negative correlations with both WR (−0.82) and COF (−0.87), validating its inverse relationship with tribological degradation. In contrast, normal load exhibits positive correlations (WR: 0.52, COF: 0.43), indicating its role in intensifying material loss via adhesive interactions.

The performance metrics in Table 6 reaffirm the accuracy of the stacked ensemble model. For COF, the model achieved an R^2 of 0.948, with a low MSE of 0.00050, RMSE of 0.0224, and MAE of 0.00275, indicating excellent predictive reliability. For WR, an R^2 of 0.908 and RMSE of 1.643 confirm strong predictive performance, despite higher variability in wear data. The MAE of 0.3111 reflects consistent prediction accuracy. These results validate the model's robustness and suitability for process-driven optimization in $AZ91/TiB_2$ composites under varied tribological conditions.

The integration of polynomially enhanced ensemble learners with a meta-learner has effectively captured the intricate relationships between process variables and tribological outcomes in $AZ91/TiB_2$ composites. This SEL approach not only improves predictive fidelity but also facilitates deeper understanding of process-structure-property linkages, offering a potent tool for intelligent material design.

Several recent studies have demonstrated the efficacy of machine learning (ML) models in accurately predicting wear behavior in magnesium matrix composites, reinforcing the approach adopted in the present work. For instance, S. S. Harish Kruthiventi[33] reported that the Decision Tree (DT) model outperformed Artificial Neural Networks (ANN) and Adaptive Neuro-Fuzzy Inference Systems (ANFIS) in predicting wear rate for AZ91 composites under optimized tribological conditions. Similarly, Reham Fathi[50] showed that the Light Gradient Boosting Machine (LightGBM) model yielded superior prediction accuracy for wear behavior in functionally graded Mg composites reinforced with eggshell particles, surpassing deeper neural networks in both speed and generalization capability. In another study, Sandeep Ganesh Mukunda[51] demonstrated the high predictive fidelity of the XGBoost model for AZ31/MWCNT composites, achieving an R^2 of 0.999 in training and 0.908 in testing—highlighting its robustness in low-data regimes typical of experimental tribological studies.

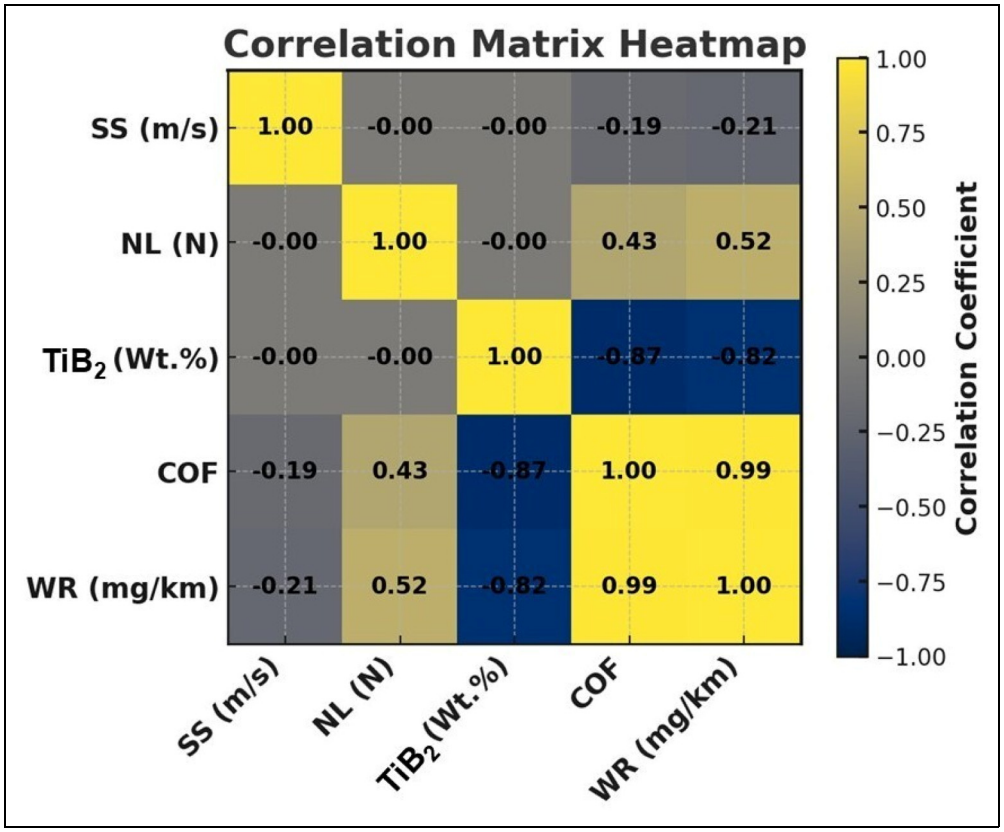

Figure 10. Correlation coefficient matrix.

Furthermore, Gajanan Anne[52] confirmed that ANN-based modeling accurately captured the wear behavior of AZ61 processed under different friction stir processing conditions, where the FSP1 variant achieved the lowest wear loss (0.003 g) and COF (0.28). Complementing these, R. Vaira Vignesh[53] applied a Sugeno–Fuzzy logic model to AZ91D alloys, revealing wear trends that mirrored physical observations, namely, increased wear at lower loads and higher speeds.

These findings collectively validate the use of advanced ML techniques in modeling wear responses and align with the outcomes of the current study, where a stacked ensemble learning (SEL) model integrating Random Forest, Gradient Boosting, and polynomial meta-regression achieved high predictive accuracy ($R^2 = 0.948$ for COF and 0.908 for WR). Notably, the SEL model demonstrated improved generalization over single learners by capturing complex nonlinear interactions between TiB_2 content, load, and sliding speed. The present study extends these earlier contributions by embedding the SEL model within a Bayesian Optimization framework, enabling both accurate prediction and multi-objective optimization of tribological parameters, thereby offering a scalable, AI-assisted design strategy for high-performance Mg-based composites.

Table 6. Performance metrics of stacked ensemble model.

Response	R^2	MSE	RMSE	MAE
COF	0.948	0.00050	0.0224	0.00275
WR	0.908	2.70	1.643	0.3111

Bayesian optimization

In multi-objective material design, especially in tribological systems like AZ91/TiB_2 composites, identifying a process window that simultaneously minimizes wear rate (WR) and coefficient of friction (COF) is non-trivial due to the complex, non-linear interdependencies among process parameters. Bayesian optimization (BO) emerges as a powerful surrogate-assisted technique, offering an efficient trade-off between exploration and exploitation by leveraging probabilistic modeling. Unlike brute-force grid searches or gradient-based optimizers, BO intelligently samples the parameter space based on posterior acquisition functions, reducing computational cost while targeting global optima.

The BO framework developed in this study was built atop a Gaussian process regression (GPR) model trained using the full experimental dataset. The inputs included sliding speed, normal load, and TiB_2 content, while the outputs were WR and COF. The optimization goal was to identify parameter configurations that minimize both responses under varying objective weights. The acquisition strategy employed was Expected improvement (EI), which balances confidence and predicted performance. The BO algorithm was iteratively executed for different objective weight combinations, denoted as (w_1, w_2), representing the importance assigned to COF and WR, respectively. The predictive accuracy of the underlying GPR model was validated using actual vs. predicted plots shown in Figure 11. The R^2 values of 0.978 for WR and 0.983 for COF highlight the high fidelity of the surrogate model in capturing the experimental behavior. The proximity of the data points to the ideal line reinforces

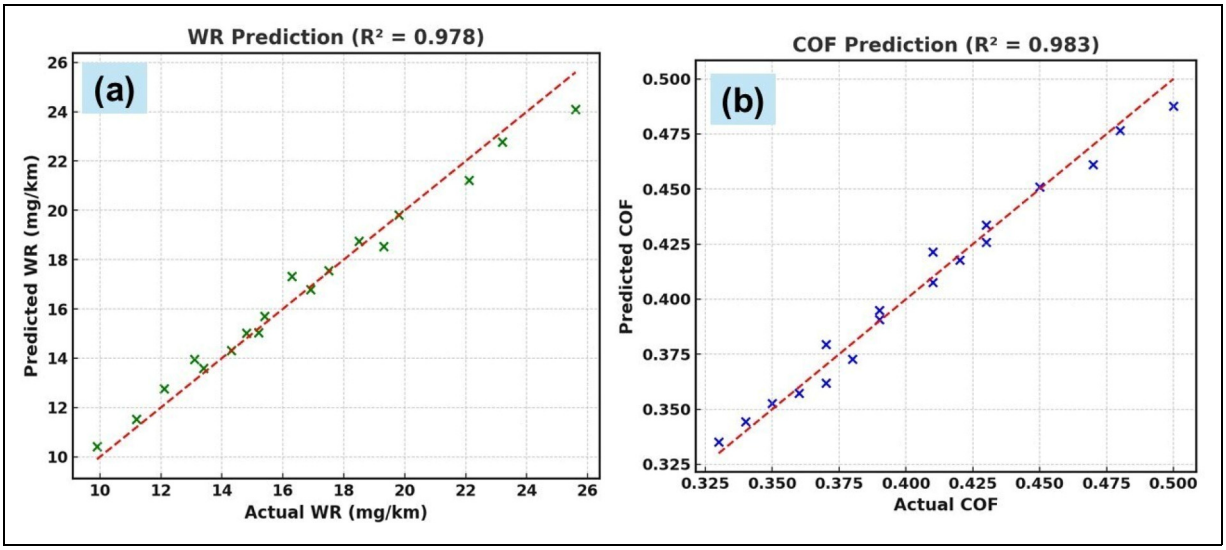

Figure 11. Actual vs predicted values of Bayesian optimization (a) wear rate (b) coefficient of friction.

Table 7. Process parameters minimized WR and COF for varying objective weights.

Weights (w_1, w_2)	Optimum (COF, WR)	Found Params (Load, Speed, TiB_2)
(1.0, 0.0)	(0.3362, 10.5740)	(12.57 N, 1.99 m/s, 3.94 wt.%)
(0.75, 0.25)	(0.3362, 10.5740)	(13.77 N, 1.94 m/s, 3.98 wt.%)
(0.50, 0.50)	(0.3362, 10.5740)	(13.77 N, 1.94 m/s, 3.98 wt.%)
(0.25, 0.75)	(0.3362, 10.5740)	(13.77 N, 1.94 m/s, 3.98 wt.%)
(0.0, 1.0)	(0.3362, 10.5740)	(13.77 N, 1.94 m/s, 3.98 wt.%)

the model's generalizability and its suitability for robust optimization.

Optimization results for varying objective weight distributions are presented in Table 7. Notably, the optimal parameter set remains consistent for all weight combinations prioritizing WR ($w_2 \neq 0$), yielding a TiB_2 content of 3.98 wt.%, a normal load of 13.77 N, and a sliding speed of 1.94 m/s, with minimal variations in COF and WR. This convergence suggests that the search space landscape for WR is more dominant, likely due to its higher sensitivity to TiB_2 particle pullout and load distribution. Conversely, the slightly different configuration at $(w_1, w_2) = (1.0, 0.0)$ focused solely on COF, identifies a lower load of 12.57 N, indicative of COF's greater responsiveness to interfacial shear characteristics at reduced mechanical stress.

The BO approach not only accelerated the discovery of optimal settings but also provided process insights into the dominance hierarchy of parameters. This capability is critical for enabling data-driven design of magnesium-based composites, facilitating application-specific tuning of tribological behavior while maintaining a sustainable experimental burden.

Compared to conventional Genetic Algorithms (GAs), Bayesian Optimization (BO) demonstrated significantly higher computational efficiency and convergence speed in the current study. BO required fewer than 20 iterations to identify optimal process parameters with high predictive confidence, leveraging a probabilistic surrogate model (Random Forest Regressor) and an Expected Improvement acquisition function to strategically sample the parameter space. In contrast, GAs typically required more than 100 iterations and larger population sizes to achieve convergence toward similar objective function values. Moreover, GAs relies on stochastic genetic operators, crossover, mutation, and selection, which often result in redundant evaluations and less sample-efficient exploration, especially in low-dimensional problems with costly experimental trials. BO, by contrast, provides a model-driven search strategy that balances exploration and exploitation, making it particularly advantageous for small-to-medium datasets where minimizing the number of experiments is critical. This efficiency gains not only reduced computational burden but also helped accelerate the experimental validation cycle, underscoring BO's practical utility for real-world materials optimization tasks.

The effectiveness of optimization frameworks in tailoring the tribological performance of magnesium matrix composites has been well-documented in the literature. For example, B. M. Girish[54] utilized the Taguchi method to investigate the wear behavior of AZ91-based hybrid composites reinforced with SiC and graphite, identifying load, speed, and reinforcement content as the most significant factors influencing wear, as determined through signal-to-noise (S/N) ratios and ANOVA. In a more advanced study, Sabbah Ataya[55] applied Response Surface Methodology (RSM) using a Face-Centered Composite Design to optimize AZ91 alloys reinforced with short carbon fibers (SCFs). Their model successfully minimized wear rate and identified fiber orientation as a critical parameter affecting surface roughness and resistance to wear.

Similarly, Vignesh Packkirisamy[56] adopted a hybrid RSM–Genetic Algorithm (GA) approach to optimize the

Table 8. Confirmation test results.

Parameters	Bayesian predicted values	Experimental values	Deviation (%)
Factors - Normal load – 13.77 N, Sliding speed – 1.94 m/s, TiB_2 (wt.%) – 3.98%			
Wear rate (mg/km)	10.574	10.235	3.2
Coefficient of friction	0.3362	0.326	2.76

wear behavior of AZ31–YSZ composites. This method led to a significantly reduced wear rate (0.0144 g/m), effectively minimizing mechanisms such as ploughing and delamination under optimized input conditions. In a parallel direction, Samar El-Sanabary[57] used GA, hybrid DOE–GA, and Multi-Objective Genetic Algorithms (MOGA) to optimize Equal Channel Angular Pressing (ECAP) parameters for Mg–Zn–Ca alloys. Their work achieved up to 56% reduction in volume loss and stabilized COF values (0.30–0.45), further supported by machine learning-based predictions and ANOVA validation.

These studies confirm that optimization tools like Taguchi, RSM, and GA are capable of identifying key parameters that govern tribological responses in Mg alloys. However, most rely on deterministic modeling or evolutionary heuristics with relatively high computational costs and limited scalability. The present study advances this landscape by employing **Bayesian** Optimization (BO) coupled with Gaussian Process Regression (GPR), enabling a probabilistically guided, sample-efficient search for optimal process conditions. Compared to conventional approaches, BO required fewer than 20 iterations to converge, accurately predicting the optimal combination of 13.77 N load, 1.94 m/s speed, and 3.98 wt.% TiB_2, achieving a low wear rate of 10.235 mg/km and COF of 0.326. These findings underscore the superiority of BO for rapid, data-driven optimization in small experimental datasets and highlight its capacity to guide the design of high-performance Mg-based composites under multi-objective constraints.

Confirmation test and characterization of wear mechanism

The confirmation test was carried out using the process parameters identified for minimizing the friction and wear properties through Bayesian Optimization: normal load of 13.77 N, sliding speed of 1.94 m/s, and TiB_2 reinforcement of 3.98 wt.%. This configuration was predicted to simultaneously minimize wear rate (WR) and coefficient of friction (COF). Experimental validation yielded WR and COF values of 10.235 mg/km and 0.326, respectively, compared to the predicted values of 10.574 mg/km and 0.3362, as shown in Table 8. The deviations of 3.2% for WR and 2.76% for COF confirm the accuracy of the Bayesian surrogate-assisted model and underscore its utility in guiding process optimization for tribologically efficient composites.

Scanning Electron Microscopy (SEM) was employed to examine the worn surface of the specimen under conditions minimized friction and wear properties. After completing confirmation test, the specimens were cleaned with acetone to remove loose debris and surface contaminants. The wear scars were then examined using a ZEISS EVO 18 Scanning Electron Microscope (SEM) operated at an accelerating voltage of 10.00 kV. The working distance ranged from 8.2 mm to 9.1 mm, and images were captured at magnifications between 500× and 2000×.

The worn surface morphologies of the AZ91/TiB_2 composite tested under optimized conditions (normal load: 13.77 N, sliding speed: 1.94 m/s, TiB_2 content: 3.98 wt.%) are shown in Figure 12(a) to (f). These SEM micrographs provide insight into the surface damage features and material removal modes governing friction and wear behavior during dry sliding. In Figure 12(a), parallel grooves aligned with the sliding direction, along with a delaminated surface flake, indicate that mild abrasive wear is a dominant mechanism. The uniformity and shallowness of these grooves suggest that the material removal is controlled, likely moderated by the presence of hard TiB_2 reinforcements which act to resist ploughing and prevent deeper penetration by counterface asperities.

Figure 12(b) exhibits adhesive pits and surface striations, which are commonly associated with local junction formation and rupture between the composite and counterface. The relatively small size and intermittent distribution of these pits point to weak adhesion tendencies, possibly mitigated by the high interfacial hardness and thermal stability of TiB_2 particles that interrupt adhesion-prone regions and promote load partitioning.

In Figure 12(c), regions of increased brightness and morphological irregularity are observed. These features are conservatively interpreted as surface contrast variations associated with localized thermal exposure during sliding. The irregular texture and brightness suggest regions where the matrix may have undergone microstructural disturbance due to elevated contact temperatures. Such localized thermal effects are typical in areas subjected to repetitive contact stress and frictional heat generation. The confined and non-continuous nature of these features indicates that thermal softening, if present, was limited in extent and likely moderated by the thermal stability of the TiB_2 reinforcement.

Figure 12(d) reveals smeared matrix regions with entrapped wear debris. Such features indicate localized plastic deformation under contact stress and the presence of third-body particles formed from micro-fractured material. The smearing suggests ductile surface behavior rather than brittle delamination, consistent with the AZ91 alloy's moderate ductility and the stabilizing influence of the reinforcement phase.

Figure 12(e) shows a particle pull-out region and surrounding deformed zone. These are indicative of reinforcement–matrix interfacial stress, where localized overloads or interfacial weakness can cause particle dislodgement. The limited extent of such features implies overall effective

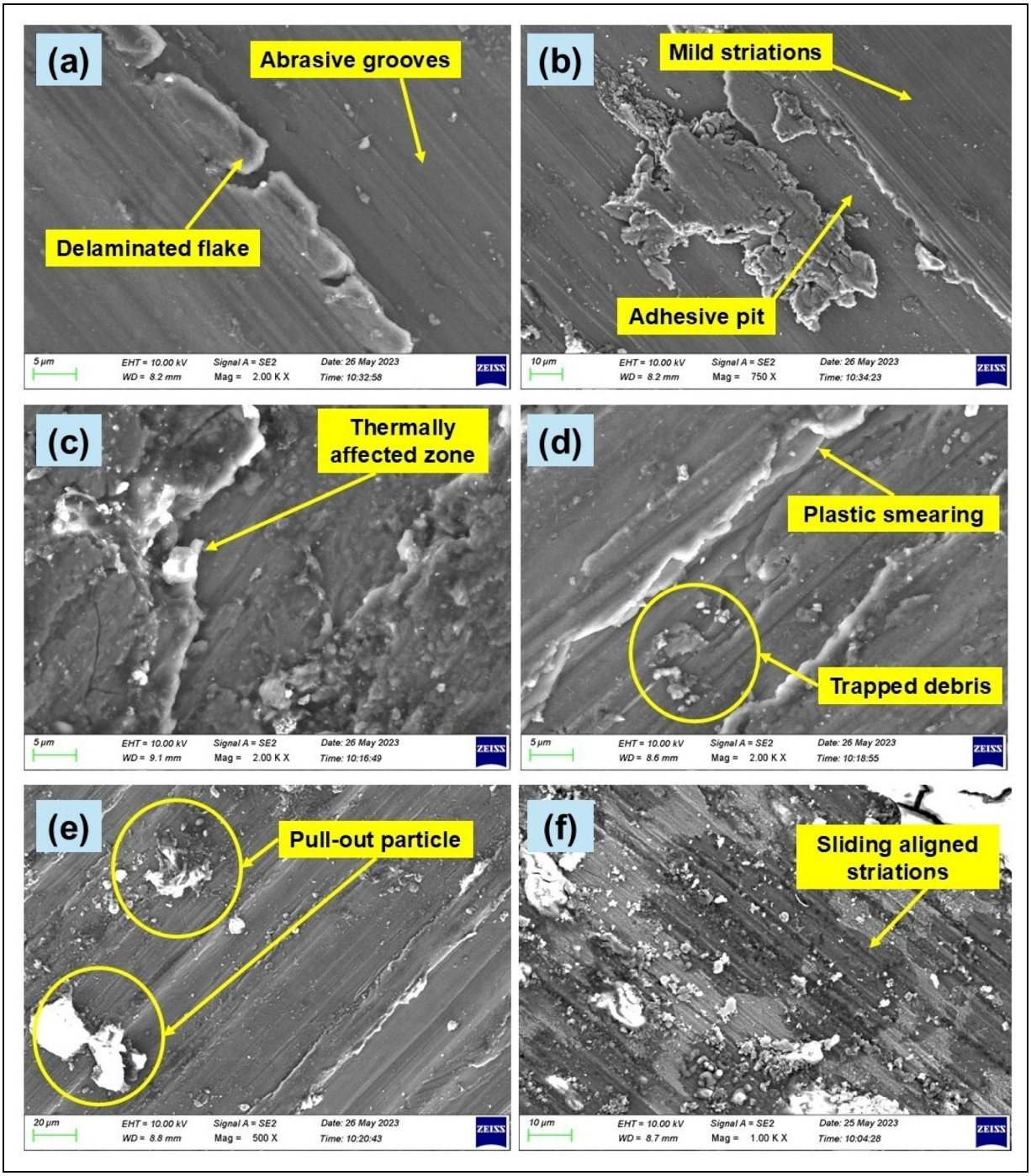

Figure 12. SEM images of worn surface of AZ91/TiB_2 composite under optimized conditions (13.77 N, 1.94 m/s, 3.98 wt.% TiB_2): (a) shallow grooves and flake; (b) striations and adhesive pit; (c) thermally affected zone; (d) plastic smear and debris; (e) pull-out feature; (f) aligned striations.

bonding between TiB_2 and the matrix, consistent with the reinforcement's angular geometry and wettability under optimized processing.

In Figure 12(f), the worn surface exhibits well-defined, sliding-aligned striations that are consistent with the direction of sliding motion. These surface features indicate a dominant shear-driven deformation mechanism, wherein the matrix undergoes localized plastic flow in response to repeated tangential loading. The regularity and continuity of these striations reflect a stable tribological interface, where the material experiences repetitive shear without abrupt mechanical instability. This behavior is attributed to the presence of uniformly dispersed TiB_2 reinforcements, which act as barriers to dislocation movement and distribute the applied stress more evenly across the matrix. Such reinforcement-assisted load sharing minimizes excessive wear and promotes the development of a streamlined, strain-hardened interface, contributing to the observed reduction in wear rate and friction coefficient under the optimized test conditions.

Altogether, the observed features support a wear mechanism dominated by mild abrasion and intermittent adhesion, with limited plastic flow and localized particle dislodgement. The absence of large-scale spalling or severe damage zones reflects the effectiveness of TiB_2 in enhancing surface

stability, distributing contact stress, and minimizing friction-induced deterioration. This microstructural behavior aligns well with the low wear rate and COF values obtained under the predicted optimal conditions.

To contextualize and reinforce the observed wear mechanisms, several similar studies in the literature provide supportive evidence. For instance, Dinesh Kumar et al. reported that the incorporation of 3 wt.% TiB_2 into AZ91D Mg alloy significantly improved wear resistance by suppressing mechanisms such as adhesion, oxidation, and delamination. This enhancement was attributed to the uniform particle distribution facilitated by ultrasonic-assisted stir casting, a processing technique also employed in the present study.[30,38]

These findings align closely with the wear behavior observed in the current AZ91/TiB_2 composites. Under optimized conditions (3.98 wt.% TiB_2, 13.77 N, 1.94 m/s), the worn surface morphology confirmed the dominance of mild abrasion, limited adhesive wear, and evidence of delamination, particularly striated regions and localized plastic smearing. Similar to the literature, the TiB_2 particles acted as micro-barriers, resisting plastic deformation and reducing matrix penetration by asperities. The presence of thermally stable TiB_2 also mitigated friction-induced softening, consistent with localized thermal zones seen in SEM images. Thus, the current study not only validates but extends previous findings by quantitatively optimizing the tribological parameters through Bayesian modeling, confirming that TiB_2 reinforcements, especially when uniformly dispersed, can effectively govern wear behavior via mechanisms such as delamination, load partitioning, and suppression of adhesive wear.

Conclusions

This study presents a robust experimental–computational approach to optimize the tribological performance of AZ91 magnesium matrix composites reinforced with TiB_2 ceramic particles. Composites were synthesized using ultrasonic-assisted stir casting, resulting in uniform reinforcement dispersion and refined microstructures. The incorporation of TiB_2 (up to 4 wt.%) significantly enhanced Brinell hardness (from 63 to 74 BHN), increased density, and reduced porosity (from 1.66% to 1.05%), contributing to improved surface integrity.

Taguchi L18 orthogonal array analysis identified TiB_2 content as the most dominant factor affecting wear rate (WR) and coefficient of friction (COF), followed by normal load and sliding speed. Experimental results demonstrated a consistent reduction in WR (up to 44.7%) and COF (up to 34.8%) with increasing TiB_2 content. Interaction plots and time-resolved COF profiles further confirmed the synergistic effects of process parameters in modulating tribological response.

A stacked ensemble learning (SEL) model integrating Random Forest, Gradient Boosting, and polynomial meta-regression yielded high prediction accuracies ($R^2 = 0.948$ for COF and 0.908 for WR), outperforming individual regressors. Bayesian Optimization, implemented via Gaussian Process Regression, successfully identified optimal parameters (13.77 N load, 1.94 m/s speed, 3.98 wt.% TiB_2), with experimentally validated outcomes (10.235 mg/km WR and 0.326 COF) showing <5% deviation from predictions. SEM analysis of worn surfaces under optimized conditions revealed shallow abrasion grooves, plastic smearing, minimal adhesive pits, and evidence of thermally stable TiB_2 particles resisting deformation and load-induced damage. The combined mechanical, statistical, and microstructural evidence validates the reinforcement's efficacy in enhancing wear resistance.

This work establishes a scalable AI-integrated methodology for designing high-performance, lightweight Mg-based composites tailored for aerospace and automotive applications. Future investigations may focus on hybrid reinforcements, in-situ ML-based wear prediction systems, and dynamic loading conditions to further improve functional performance and reliability.

ORCID iDs

Hariharasakthisudhan Ponnarengan https://orcid.org/0000-0002-9420-3196

Sathickbasha Katharbasha https://orcid.org/0000-0001-8974-154X

Author contributions

- **Sathish K** – Investigation, Data Curation, Methodology, Writing – Original Draft
- **Baskar S** – Conceptualization, Supervision, Project Administration, Validation
- **Ponnarengan Hariharasakthisudhan** – Writing – Review & Editing, Formal Analysis, Visualization
- **Kamaraj Logesh** – Software, Modeling, Resources, Validation
- **Sathickbasha K** – Experimental Setup, Data Curation, Writing – Review & Editing

Funding

The authors received no financial support for the research, authorship, and/or publication of this article.

Declaration of conflicting interests

The authors declared no potential conflicts of interest with respect to the research, authorship, and/or publication of this article.

Data availability statement

The data supporting the findings of this study are available from the corresponding author upon reasonable request.

References

1. Gupta M and Wong WL. Magnesium-based nanocomposites: lightweight materials of the future. *Mater Charact* 2015; 105: 30–46.
2. Mitra A, Mandal SK and Rai RN. Synthesis and characterisation of magnesium-based nano-composite–A review. *Proc Inst Mech Eng Part E J Process Mech Eng* 2024; 238: 2994–3008.
3. Krstić J, Jovanović J, Gajević S, et al. Application of metal matrix nanocomposites in engineering. *Adv Eng Lett* 2024; 3: 180–190.

4. Kumar KCK, Kumar BR and Rao NM. Artificial neural network modeling of tribological parameters optimization of AZ31-SiC metal matrix composite. *Appl Eng Lett* 2023; 8: 111–120.
5. Sharma SK, Gajević S, Sharma LK, et al. Magnesium-titanium alloys: a promising solution for biodegradable biomedical implants. *Materials (Basel)* 2024; 17: 5157.
6. Vencl A. Tribology of the al-si alloy based MMCs and their application in automotive industry. In: Engineered metal matrix composites: forming methods, material properties and industrial applications. 2013, pp.127–166. https://hdl.handle.net/21.15107/rcub_machinery_1807.
7. Sannino AP and Rack HJ. Dry sliding wear of discontinuously reinforced aluminum composites: review and discussion. *Wear* 1995; 189: 1–9.
8. Vencl A, Rac A, Bobić I, et al. Tribological properties of Al-Si alloy A356 reinforced with Al_2O_3 particles. *Tribol Ind* 2006; 28: 27–31.
9. Patle H, Sunil BR, Kumar SA, et al. Effects of inert gas environment on the sliding wear behavior of AZ91/B_4C surface composites. *Proc Inst Mech Eng Part J J Eng Tribol* 2021; 236: 1880–1888.
10. Aatthisugan I and Murugesan R. Optimization of wear and friction behaviour of AZ91-B_4C-Gr hybrid composite under dry sliding conditions. *Proc Inst Mech Eng Part J J Eng Tribol* 2022; 237: 775–783.
11. Niranjan CA, Shobha R, Prabhuswamy NR, et al. Reciprocating dry sliding wear behaviour of AZ91/Al_2O_3 magnesium nanocomposites. *Arab J Sci Eng* 2024; 49: 2299–2310.
12. Zarghami M, Emamy M, Malekan M, et al. Dry sliding wear behaviour of AZ91–Mg_2Si–SiC hybrid composites at elevated temperatures. *Mater Sci Technol* 2023; 39: 1021–1029.
13. Kumar A, Kumar S, Mukhopadhyay NK, et al. Effect of TiC reinforcement on mechanical and wear properties of AZ91 matrix composites. *Int J Metalcasting* 2022; 16: 2128–2143.
14. Raj PP, Vijayakumar P, Ramadoss N, et al. Experimental investigation of the microstructural and wear behaviours of silicon carbide and boron nitride-reinforced AZ91D magnesium matrix hybrid composites. *J Braz Soc Mech Sci Eng* 2024; 46: 536.
15. Kumar D and Thakur L. A study of development and sliding wear behavior of AZ91D/Al_2O_3 composites fabricated by ultrasonic-assisted stir casting. *Arab J Sci Eng* 2023; 48: 2951–2967.
16. Zarghami M, Emamy M and Malekan M. Microstructure, mechanical properties and wear behaviour of the AZ91–Mg_2Si–SiC hybrid composites. *Mater Sci Technol* 2021; 37: 1333–1341.
17. Abdollahzadeh A, Bagheri B, Abbasi M, et al. Mechanical, wear and corrosion behaviors of AZ91/SiC composite layer fabricated by friction stir vibration processing. *Surf Topogr Metrol Prop* 2021; 9: 035038.
18. Bharathi ML, Rag SA, Chitra L, et al. Investigation on wear characteristics of AZ91D/nanoalumina composites. *J Nanomater* 2022; 2022: 2158516.
19. Gnanavelbabu A, Vinothkumar E, Ross NS, et al. Investigating the wear performance of AZ91D magnesium composites with ZnO, MnO, and TiO_2 nanoparticles. *Int J Adv Manuf Technol* 2023; 129: 4217–4237.
20. Xiao P, Gao Y, Sheng Y, et al. Improving wear and corrosion resistances of Mg_2Si/AZ91 composites via tailoring microstructure and intrinsic properties of Mg_2Si induced by Sb modification. *J Magnes Alloy* 2024; 12(11): 4493–4508.
21. Singh S and Chauhan NR. Optimization of adhesive wear behaviour of B_4C/AZ91D-Mg composites. *Adv Mater Process Technol* 2022; 8: 4058–4072.
22. Goodarzi M, Malekan M and Emamy M. Effect of CNTs on microstructure, mechanical and wear properties of the AZ91–3B_4C–3SiC–x CNTs composites. *Mater Sci Technol* 2024; 40: 1058–1068.
23. Fountas NA, Kechagias JD and Vaxevanidis NM. Swarm intelligence algorithms for optimising sliding wear of nanocomposites. *Tribol Mater* 2024; 3: 44–50.
24. Stojanović B, Gajević S, Kostić N, et al. Optimization of parameters that affect wear of A356/Al_2O_3 nanocomposites using RSM, ANN, GA and PSO methods. *Ind Lubr Tribol* 2022; 74: 350–359.
25. Vencl A, Svoboda P, Klančnik S, et al. Influence of Al_2O_3 nanoparticles addition in ZA-27 alloy-based nanocomposites and soft computing prediction. *Lubricants* 2023; 11: 24.
26. Akuwueke LM, Ossia CV and Nwosu HU. Surface texturing for tribomechanical performance optimisation of epoxy composites reinforced with chemically activated carbon. *Tribol Mater* 2024; 3: 150–162.
27. Xiao P, Gao Y, Xu F, et al. Tribological behavior of in-situ nanosized TiB_2 particles reinforced AZ91 matrix composite. *Tribol Int* 2018; 128: 130–139.
28. Sahoo BN and Panigrahi SK. Development of wear maps of in-situ TiC+TiB_2 reinforced AZ91 Mg matrix composite with varying microstructural conditions. *Tribol Int* 2019; 135: 463–477.
29. Sui X, Xu H, Jiang B, et al. Effect of the TiB_2 content on the mechanical and tribological properties of TiB_2/AZ91 composites fabricated by vacuum hot-press sintering process incorporating vacuum ball milling. *Mater Today Commun* 2024; 40: 109722.
30. Kumar D and Thakur L. Wear performance of TiB_2-reinforced AZ91 magnesium metal matrix composite fabricated by ultrasonic stir-casting process. *JOM* 2023; 75: 2731–2744.
31. Cevik E and Gundogan M. Dry sliding wear behavior of (GNPs+TiB_2)-reinforced AZ91 magnesium matrix hybrid composites produced by pressure infiltration casting method. *Int J Metalcasting* 2021; 15: 1250–1259.
32. Sahoo SK, Ramesh MR and Panigrahi SK. Establishing high temperature tribological performance and wear mechanism map of engineered in-situ TiB_2 reinforced Mg-RE metal matrix composites. *Tribol Int* 2025; 201: 110189.
33. Kruthiventi SH and Ammisetti DK. Experimental investigation and machine learning modeling of wear characteristics of AZ91 composites. *J Tribol* 2023; 145: 101704.
34. Mishra A, Jatti VS and Sefene EM. Exploratory analysis and evolutionary computing coupled machine learning algorithms for modelling the wear characteristics of AZ31 alloy. *Mater Today Commun* 2023; 37: 107507.
35. Macit CK, Saatci BT, Albayrak MG, et al. Prediction of wear amounts of AZ91 magnesium alloy matrix composites reinforced with ZnO–hBN nanocomposite particles by hybridized GA–SVR model. *J Mater Sci* 2024; 59: 17456–17490.
36. Aydin F and Durgut R. Estimation of wear performance of AZ91 alloy under dry sliding conditions using machine

learning methods. *Trans Nonferrous Met Soc China* 2021; 31: 125–137.
37. Pasha MB, Rao RN, Ismail S, et al. Tribo-informatics approach to predict wear and friction coefficient of Mg/Si_3N_4 composites using machine learning techniques. *Tribol Int* 2024; 196: 109696.
38. Kumar D and Thakur L. A study of processing and parametric optimization of wear-resistant AZ91–TiB_2 composite fabricated by ultrasonic-assisted stir casting process. *Surf Topogr Metrol Prop* 2022; 10: 025024.
39. Mathivanan K, Thirumalaikumarasamy D, Ashokkumar M, et al. Optimization and prediction of AZ91D stellite-6 coated magnesium alloy using box–Behnken design and hybrid deep belief network. *J Mater Res Technol* 2021; 15: 2953–2969.
40. Veera Ajay C, Manisekar K, Andrews A, et al. Optimization and prediction of the tribological parameters of biocompatible AZ31/Al_2O_3/Si_3N_4 metal matrix composites using CCD–RSM, MOORA and FNN models. *Int J Interact Des Manuf* 2025: 1–22.
41. Vignesh C, Chockalingam K, Umar Sherif S, et al. Predicting and optimizing the wear behavior of centrifugal cast β-TCP/Mg–2Zn–1Mn alloys: A hybrid artificial neural network–Grey relational analysis approach. *Proc Inst Mech Eng Part E J Process Mech Eng* 2024. Epub ahead of print 9 December 2024. DOI: 10.1177/09544089241300003.
42. Kumar S and Gupta RN. Tribological study of magnesium-based AZ91/TiC/rGO hybrid composite prepared by powder metallurgy route: an experimental and analytical approach. *Adv Mater Process Technol* 2024; 11(02): 1136–1155.
43. Xia Y, He Z and Feng X. Stacking ensemble learning framework for predicting tribological properties and optimal additive ratios of amide-based greases. *Friction* 2025; 13(07): 9440982.
44. Xia Y, Cheng X, Feng X, et al. Research on a stacking ensemble model with adaptive feature weighting for predicting the tribological properties of lubricating grease. *J Tribol* 2025; 147: 114502.
45. Kumaravel S and Suresh P. Ensemble machine learning for predicting and enhancing tribological performance of Al5083 alloy with HEA reinforcement. *Proc Inst Mech Eng Part J J Eng Tribol* 2025. Epub ahead of print 10 January 2025; 239(07): 839–860.
46. Hulipalled P, Algur V, Lokesha V, et al. Interpretable ensemble machine learning framework to predict wear rate of modified ZA-27 alloy. *Tribol Int* 2023; 188: 108783.
47. Mi X, Dai L, Jing X, et al. Accelerated design of high-performance Mg–Mn-based magnesium alloys based on novel Bayesian optimization. *J Magnes Alloy* 2024; 12: 750–766.
48. Ghorbani M, Boley M, Nakashima PN, et al. An active machine learning approach for optimal design of magnesium alloys using Bayesian optimisation. *Sci Rep* 2024; 14: 8299.
49. Peng P, Peng Y, Liu F, et al. Bayesian optimization and explainable machine learning for high-dimensional multi-objective optimization of biodegradable magnesium alloys. *J Mater Sci Technol* 2025; 238: 132–145.
50. Fathi R, Chen M, Abdallah M, et al. Wear prediction of functionally graded composites using machine learning. *Materials (Basel)* 2024; 17: 4523.
51. Mukunda SG, Srivastava A, Boppana SB, et al. Wear performance prediction of MWCNT-reinforced AZ31 composite using machine learning technique. *J Bio Tribo-Corros* 2023; 9: 27.
52. Anne G, Ramesh S, Sharma P, et al. Enhancing wear resistance of AZ61 alloy through friction stir processing: experimental study and prediction model. *Mater Res Express* 2024; 11: 056524.
53. Vignesh RV and Padmanaban R. Forecasting tribological properties of wrought AZ91D magnesium alloy using soft computing model. *Russ J Non-Ferrous Met* 2018; 59: 135–141.
54. Girish BM, Satish BM, Sarapure S, et al. Optimization of wear behavior of magnesium alloy AZ91 hybrid composites using taguchi experimental design. *Metall Mater Trans A* 2016; 47: 3193–3200.
55. Ataya S, Alrasheedi NH, Seleman MME, et al. Response surface methodology-based optimization of AZ91 composites reinforced with short carbon fibers for enhanced mechanical and wear properties. *Processes* 2025; 13: 1697.
56. Packkirisamy V, Thirugnanasambandam A, Bhowmik A, et al. Synergistic approach to wear rate forecasting in AZ31/5% yttria stabilized zirconia reinforced composite through response surface methodology-genetic algorithm integration. *Proc Inst Mech Eng Part J J Eng Tribol* 2025; 239: 189–199.
57. El-Sanabary S, Kouta H, Shaban M, et al. A comparative study of machine learning and response surface methodologies for optimizing wear parameters of ECAP-processed ZX30 alloy. *Heliyon* 2024; 10(13): e33967.